Novel InTlSb alloy for uncooled long-wavelength infrared photodetectors

J.J. LEE, J.D. KIM, and M. RAZEGHI[*]

Center for Quantum Devices, Department of Electrical and Computer Engineering,
Northwestern University, Evanston, Illinois 60208, USA

In this paper, we report on the growth and characterization of novel InTlSb alloys for uncooled long-wavelength infrared photodetector applications. The InTlSb epilayers were grown on InSb and GaAs substrates by low-pressure metalorganic chemical vapor deposition. The incorporation of Tl into InSb was investigated in detail with Auger electron spectroscopy, high-resolution x-ray diffraction, transmission, absorption, photoresponse measurements, and Hall effect measurements. We also demonstrate the photodetectors fabricated from the grown InTlSb alloys. Photoresponse of InTlSb photodetectors is observed up to 11 µm at room temperature. The maximum responsivity of an $In_{0.96}Tl_{0.04}Sb$ photodetector is about 6.64 V/W at 77 K, corresponding to a Johnson noise limited detectivity of 7.64×10^8 $cmHz^{1/2}W^{-1}$. The carrier lifetime in InTlSb photodetectors derived from the stationary photoconductivity is 10-50 ns at 77 K. The present results showed the feasibility of using InTlSb alloys for the uncooled infrared photodetector applications.

Keywords: InTlSb photodetectors, uncooled infrared detectors, photoconductors.

1. Introduction

Infrared detectors and imaging arrays operating in the long-wavelength infrared (8-12 µm) range have attracted much interest because of their wide range of applications in areas such as night vision, reconnaissance, infrared missile seeker-tracer systems, ranging, space surveillance, industrial thermography, medical imaging, meteorological research, and communication systems [1]. For this purpose, thermal detectors such as bolometers, pyroelectric detectors, and thermocouples can be operated at ambient temperature [2]. Uncooled thermal detectors are lightweight, rugged, reliable, and convenient to use. However, their detectivity is relatively low, especially when operated at high frequencies. A high sensitivity and fast response detection of infrared radiation can be achieved with the use of semiconductor photodetectors [3]. One of the major drawbacks of infrared photodetectors is the need for cooling to suppress thermal processes that compete with the optical ones in the generation of free carriers in a semiconductor.

The need for cooling is a considerable problem that inhibits the more wide spread use of infrared systems. The cooling requirements add considerably to the cost, bulk, weight, and power consumption, so it is highly desirable that they be eliminated. To overcome the problems originated from cryogenic cooling, there have been a lot of theoretical and experimental works to develop uncooled infrared photodetectors [4-8].

HgCdTe (MCT) has been the dominant material system for such applications. MCT offers the freedom of tailoring its band gap from the HgTe (–0.30 eV) to the CdTe (1.60 eV) by varying the Hg/Cd ratio within the crystal. However, this II-VI compound is notorious for metallurgical problems; the weak Hg-Te bonding restricts the strength of the material, and the high Hg vapor pressure makes it difficult to grow alloys with uniform composition over large substrate areas and is also the reason for poor thermal stability.

A number of novel material systems and structures based on III-V semiconductors have been proposed as alternatives of current market dominant MCT. Bulk III-V semiconductors utilising direct interband optical transition have been investigated as possible infrared materials, capable of providing the

flexibility of MCT such as simpler device structures and higher quantum efficiency but with the added metallurgical and processing advantages offered by III-V technology. These new materials include InAsSb [9-12], metastable InTlSb [13-15], InSbBi [16-21], InAsBi [22], InAsSbBi [22], InTlP [23], and InTlAs [23].

Recently, band structure calculations predicted a new semimetal, TlSb, with a band gap of −1.5 eV [13]. Also it was suggested that by alloying TlSb with InSb the band gap could be varied from −1.5 to 0.17 eV. $In_{1-x}Tl_xSb$ is expected to exhibit a similar lattice constant and structure as InSb since the radius of Tl atom is very similar to that of In. Even though, TlSb was expected to favour the CsCl-type structure, InTlSb alloy was estimated to exhibit a zinc-blende structure up to 20% Tl. Wood et al. first attempted the growth of InTlSb alloy by molecular beam epitaxy (MBE) but never succeeded in observing any change in the physical properties of InSb [24].

This study presents the physical properties of this new InTlSb alloy and the advancements made towards realising InTlSb infrared photodetectors. The first successful growth of InTlSb alloys exhibiting extended infrared photoresponse is described. Detailed discussion of various structural, optical, and electrical characterisation results are also given to gain insight into the material properties of InTlSb. In addition, the first InTlSb photodetectors are demonstrated and their detectivities are evaluated to assess the merits of InTlSb as novel III-V material for infrared detection.

2. Physical properties and growth of InTlSb alloy

2.1. Band and crystal structure of InTlSb alloy

The band structure of InTlSb has been investigated by Schilfgaarde et al. based on material parameters of its binary constituents, InSb and TlSb [13]. However, very limited experimental data is available on TlSb. One of the earliest studies was done by Williams in 1906, who first determined the fundamental Tl-Sb binary phase diagram [25]. Since then, other intermediate Tl-Sb phases have been reported [26, 27] and TlSb is found to be stable only in the narrow temperature range from 191 to 195°C but other parameters such as crystal structure and lattice constants are not experimentally known.

The material characteristics of TlSb utilised by Schilfgaarde et al. were calculated using the full potential linear muffin tin orbital method (LMTO) within local density approximation (LDA). The results of the investigation showed that TlSb slightly favours the CsCl over the zinc blende structure at zero temperature and zinc blende solid solution of InTlSb is stable at low Tl content, as illustrated in Fig. 1. Moreover, InTlSb is predicted to be more robust than HgCdTe because of higher cohesive energies of InSb and TlSb compared to those of CdTe and HgTe. In the 8-12 μm wavelength range, InTlSb has stronger bonded InSb as its majority component.

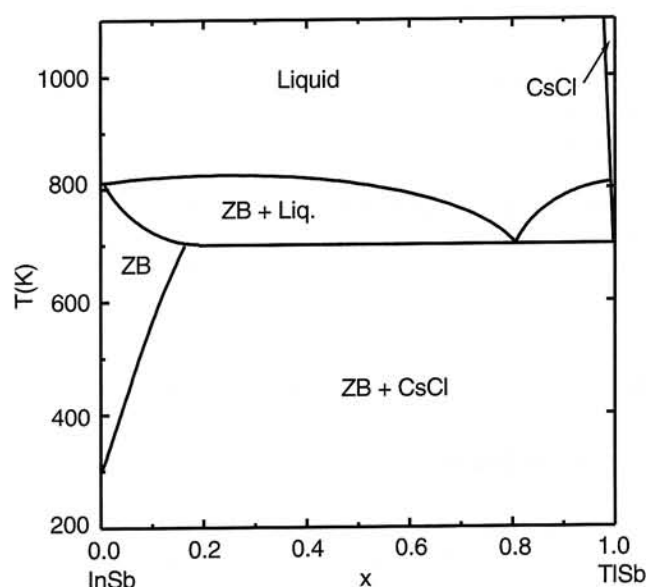Fig. 1. Phase diagram of $In_{1-x}Tl_xSb$ alloy (after Ref. 13). ZB stands for zinc blende structure.

The band gap of TlSb was determined through LDA, which is known to underestimate the semiconductor band gaps as much as 50% [28]. This uncertainty was accounted for by exploiting the systematic nature of the LDA errors; assuming that TlSb has a dielectric constant close to InSb and HgTe, the average of the underestimates of these two were used to obtain the corrected TlSb band gap of −1.5 eV [13].

Based on a scaled virtual crystal approximation (VCA) and the band gaps of TlSb and InSb, the band gap of $In_{1-x}Tl_xSb$ was calculated at zero temperature as a function of alloy composition x. The estimated x value for 0.1 eV band gap at zero temperature is x = 0.083 [13].

2.2. MOCVD growth of InTlSb epitaxial films

Low-pressure metalorganic chemical vapour deposition (LP-MOCVD) has been used as the growth technique because of its success in growing new as well as metastable materials. In order to establish the proper growth conditions for $In_{1-x}Tl_xSb$, first, optimum growth conditions for high quality InSb films were investigated [14]. InSb films were grown on InSb, GaAs, and Si substrates using trimethylindium (TMI) and trimethylantimony (TMSb) as sources of In and Sb, respectively. Growth conditions such as substrate temperature and V/III ratio were varied to obtain good quality films. Substrate temperature was varied from 425 to 475°C and V/III ratio was varied from 5 to 15. Once the growth conditions of high quality InSb were determined, growth of $In_{1-x}Tl_xSb$ was attempted. Cyclopentadienylthallium (CPTl) was used as precursor of thallium. The InTlSb epilayers were grown by introducing Tl flux into the reactor at the optimum growth conditions of InSb. Different amount of Tl flux was sent to the growth chamber to obtain InTlSb alloy with different Tl concentration. This was achieved by varying both the bubbler temperature as well as the flow rate of CPTl. The growth conditions for InTlSb are summarised in Table 1.

Table 1. Optimum growth conditions for InTlSb.

Growth temperature	455°C
Growth pressure	76 Torr
TMI flow rate	50 cc/min
TMSb flow rate	20 cc/min
CPTl flow rate	3–20 cc/min
CPTl bubbler temperature	0–80°C

3. Characterisation of InTlSb epitaxial films

3.1. Chemical analysis by Auger electron spectroscopy

Auger electron spectroscopy (AES) provides the direct information on the elements in the film. As shown in Fig. 2, the AES spectrum of an $In_{0.96}Tl_{0.04}Sb$ film grown with LP-MOCVD technique has a well resolved Tl peak at 70 eV in addition to the In and Sb peaks. The spectrum also shows a couple of peaks from carbon and oxygen that were unintentionally incorporated in the film.
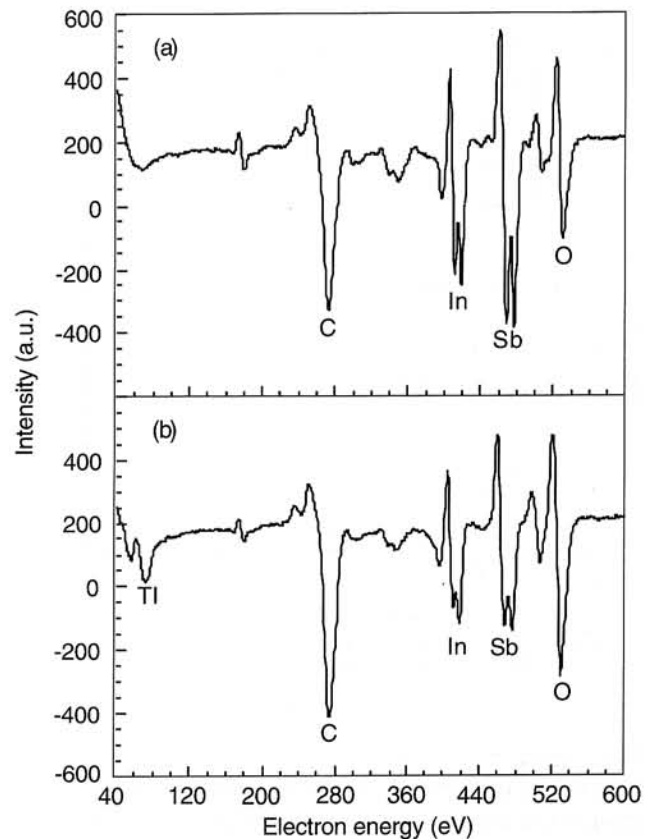

Fig. 2. Auger electron spectra of (a) InSb and (b) InTlSb sample.

3.2. Structural characteristics

Figure 3 shows the (004) high resolution x-ray diffraction (HRXRD) curves of the InSb and $In_{1-x}Tl_xSb$ layers on GaAs substrates. As expected, the x-ray peaks corresponding to the InSb epilayer and GaAs substrate were observed at an angle of 28.39° and 33.02°, respectively. A striking feature appeared in the x-ray diffraction spectra for the $In_{1-x}Tl_xSb$ films. The epilayers, which exhibited a Tl peak in AES spectrum and an extended cutoff wavelength in infrared photoresponse measurements (see Fig. 7), showed a clear shift of the x-ray diffraction peak toward the high angle with respect to that of InSb. It should be noted that the Bragg diffraction peak shifted to higher angle implies the decrease of out-of-plane lattice parameter of the $In_{1-x}Tl_xSb$ according to the Bragg's law (see the inset of Fig. 3). As Tl incorporation increased, the diffraction peaks were gradually shifted toward the high angle in the experimental range due to the decrease of out-of-plane lattice parameter of $In_{1-x}Tl_xSb$. For the zinc blende structure which forms sp^3 hybridisation, tetrahedral coordination can be assumed in the grown InTlSb since this ternary is in the
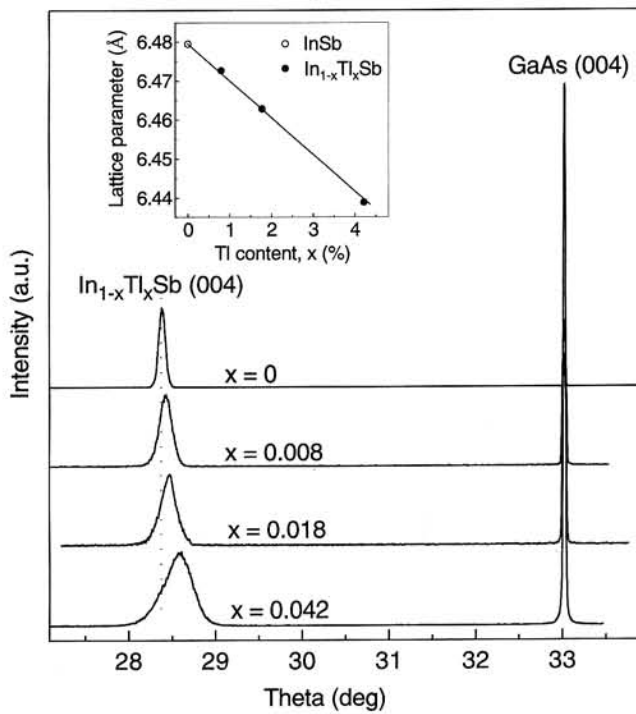
Fig. 3. Four-crystal (004) x-ray rocking curves of InSb and InTlSb samples grown on GaAs substrates. The vertical dashed line corresponds to the peak position of the InSb epilayer. The inset shows the out-of-plane lattice parameter as a function of Tl content.

high In composition region, the bond length between nearest-neighbours, i.e., lattice parameter, is proportional to the sum of tetrahedral covalent radii of constituent atoms. From the fact that the tetrahedral covalent radius of Tl is greater than that of In ($r_{In} = 1.44$ Å and $r_{Tl} = 1.47$ Å according to Pauling [29]), this unique observation cannot be accounted for by atomic size effect. At the same time, this indicates the existence of residual tensile in-plane stress in the film. Taking account of the InTlSb films under the biaxial stress, the in-plane stress can be roughly estimated by the simple expression for the elasticity theory [30],

$$\sigma_{\parallel} = \frac{|c - c_o|}{c_o} \frac{B}{v}, \qquad (1)$$

where c_o is the strain-free lattice constant of the fully relaxed lattice, B is the bulk modulus, and v is the

Poisson's ratio. As the material parameters for $In_{1-x}Tl_xSb$ are not established, many of the physical parameters such as bulk modulus, strain-free lattice constant, and Poisson's ratio needed for the stress calculation were estimated using Vegard's law. The parameters for TlSb and InSb used in this evaluation were summarised in Table 2. The physical constants for TlSb were taken from the recent theoretical study of van Schilfgaarde et al. [13]. Due to the lack of information on Poisson's ratio for TlSb, we estimated it from the following expression [30]

$$v = \frac{3B - 2(c_{11} - c_{12})}{2[3B + (c_{11} - c_{12})]}, \qquad (2)$$

where $c_{11} - c_{12}$ is the shear modulus, from which we obtain $v = 0.31$.

Figure 4 plots the tensile in-plane stress estimated by Eq. (1) and the full width at half maximum (FWHM) of HRXRD obtained from (004) reflections as a function of Tl content. The trend shows a gradual increase of residual stress by Tl incorporation in InSb. The magnitude of stress varies from 1.6×10^4 to 8.8×10^5 N/cm^2. With increasing Tl incorporation, both residual stress and FWHM of HRXRD increased in the studied range, exhibiting strong correlation between the stress and the defects. Residual stresses have previously been observed in thin film [31]. Residual tensile in-plane stress originated from the lattice parameter mismatch between the epilayer and substrate does not seem to explain the current results since the InTlSb alloys have a larger lattice constant than GaAs. The influence of free electrons on lattice also seems to be negligible in this argument since the room temperature electron concentration of InTlSb is too low (~ mid 10^{16} cm^{-3}) to substantially affect the lattice parameter via the deformation potential of a conduction band minimum [32]. The present results show that the stress may be evolved through the defects in the film resulted from the interaction between the host lattice and Tl atoms. The dependence of stress on defects seems to imply the direct correlation between the stoichiometry (i.e., vacancy and intersti-

Table 2. Material parameters for InSb and TlSb used in this analysis (after Ref. 13).

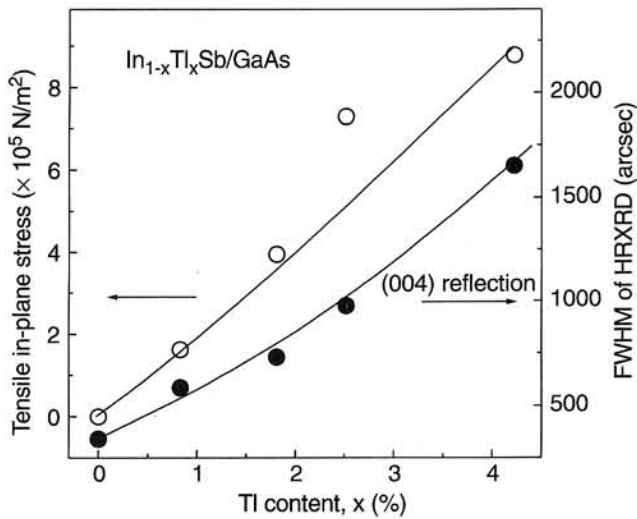|	Lattice constant (Å)	Bulk modulus (J/cm^3)	Shear modulus (J/cm^3)	Poisson's ratio
InSb	6.4794	0.45×10^5	0.31×10^5	0.34
TlSb	6.59	0.38×10^5	0.22×10^5	0.31

Fig. 4. Tensile in-plane stress and FWHM of HRXRD as a function of Tl content. The lines were drawn to guide the eye.

tial concentrations) and lattice parameter [31,33]. It should be noted that the formation of vacancies and interstitials in InTlSb system is highly probable due to the large immisciblity between InSb and TlSb under equilibrium growth conditions [13]. It is thus suggested that stoichiometric instability nurtured by point defects such as vacancies and interstitials may be, at least partially, responsible for the tensile stress [31, 33, 34]. It is noteworthy that the stress obtained is comparable to the defect-induced residual stress value for homoepitaxial $SrTiO_3$ film ($\sim 10^4$–10^5 N/cm^2) [33]. In this sense, the arguments of Du et al. that relatively large covalent radius of substitutional Bi atom (r_{Bi} = 1.46 Å [29]) would make vacancies in the host matrix (GaInSb) and limit the solubility ($\sim$ 3% for Bi) [35] agree with our statement. As another possible explanation, the differences of thermal expansion coefficients of film and substrate may give rise to the tensile thermal stress during the cool-down process [34]. However, it is a little difficult to confirm this analysis quantitatively at the present stage because of the lack of thermal expansion coefficient value for InTlSb. An experimental work for the growth of TlSb is underway to identify the precise origin.

3.3. Optical characteristics

Figure 5(a) and 5(b) show the results of optical transmission measurements of InSb and InTlSb, respectively. The absorption edge of InTlSb clearly extends beyond that of InSb (λ^{-1} = 1818 cm^{-1}). However, an accurate assessment of the absorption edge by this method is difficult due to thin epilayers and
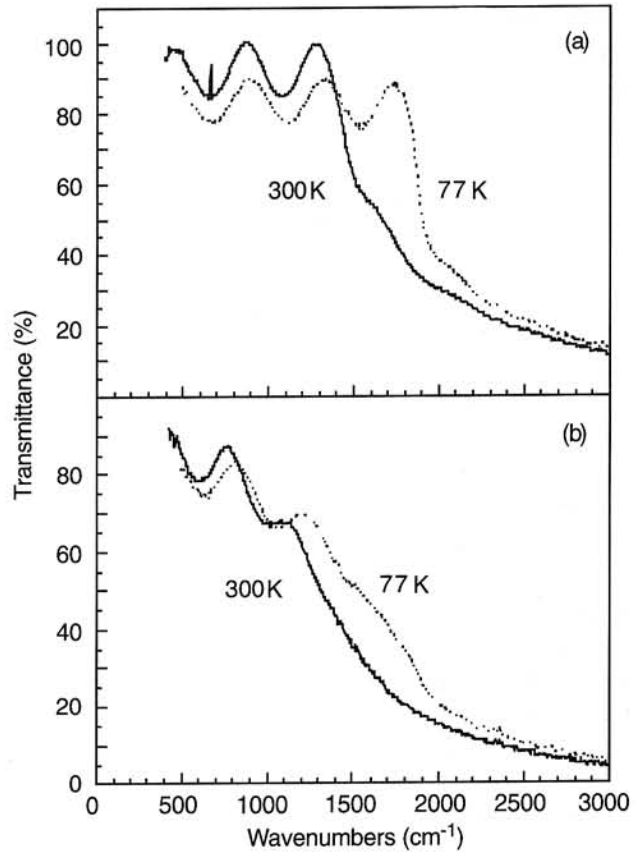

Fig. 5. Optical transmission of (a) InSb and (b) InTlSb versus wavenumber (10^4/wavelength) at 77 and 300 K.

observed Fabry-Perot oscillations. These oscillations are produced by multiple reflections at the air--epilayer and epilayer-substrate interfaces, and from their period other interesting optical parameters such as refractive index of the epilayers have been extracted [15]. The period of the oscillations yields the phase shift for light passing through the epilayer, from which the product $n \cdot d$ can be extracted, where n is the refractive index of the epilayer and d is its thickness. Assuming tabulated values for the refractive index of InSb, n = 3.9 $\pm$ 0.1 within the wavelength range of interest [36], this provides an independent estimate of the InSb epilayer thickness, d = 2.9$\pm$0.1 μm which is about the same as the value determined from ball-polishing measurement. Looking at the InTlSb/InSb spectrum, the product $n \cdot d$ appears slightly larger than for the InSb sample. No refractive index data is available for InTlSb, but since it has a smaller band gap than InSb its refractive index should be higher. However, this difference is expected to be only slight compared to the large refractive index difference between InSb and GaAs. This is confirmed by the fact that no additional interference feature that might occur from InSb/InTlSb interface is observed.

In brief, the slightly higher value of the product n · d can originate from a slight increase in the refractive index as well as from a slight difference in total layer thickness that would lie within the ball-polishing measurement uncertainty.

A careful observation of Fig. 5 reveals that the product n · d increases with temperature because the fringe spacing is slightly reduced. By recording precisely the position of the Fabry-Perot extrema and their shift with temperature, the average value of the temperature coefficient of the product n · d in the transparent wavelength range can be experimentally determined; $[1/(n \cdot d)] \, d(n \cdot d)/dT = 7.7 \times 10^{-5} \, K^{-1}$ for the InSb sample and $2.8 \times 10^{-4} \, K^{-1}$ for the InTlSb sample. It is apparent from these values that the Fabry-Perot fringes undergo a much larger change with temperature in the case of the InTlSb/InSb sample. Comparing these experimental values with tabulated values for InSb [36]; $[1/n] \cdot dn/dT = 4.5 \times 10^{-5} \, K^{-1}$ for the temperature coefficient of the refractive index and $[1/d] \cdot dd/dT = 0.5 \times 10^{-5} \, K^{-1}$ for the thermal expansion coefficient, from which we deduce

$$\frac{1}{nd}\frac{d(nd)}{dT} = \frac{1}{n}\frac{dn}{dT} + \frac{1}{d}\frac{dd}{dT} = 5.0 \times 10^{-5} K^{-1} \quad (3)$$

Note that the change in the product n · d occurs mainly through the variation of the refractive index. The experimental value is in reasonable agreement with the tabulated one in the case of InSb. No such tabulated data are available for InTlSb. One of the possible reasons for the much larger temperature dependence in the case of InTlSb is the enhanced refractive index dispersion near the absorption edge, which results in an enhanced dispersion for its temperature coefficient as well. Since fewer fringes are visible in the case of the InTlSb/InSb sample, the experimental values have been averaged over a narrower wavelength region close to the InTlSb absorption edge.

In order to determine the absorption coefficient, the epilayer has been modelled as a conventional Fabry-Perot etalon filled with an absorbing medium [15]. The reflection and transmission coefficient of each interface were determined using tabulated values for the refractive index of GaAs and InSb, and the refractive index of InTlSb was assumed to be the same as that of InSb. The phase shift through the epilayer was determined from the position of the experimental Fabry-Perot extrema. The resulting absorption spectra at 77 K are given in Fig. 6; the InSb sample exhibits a sharp absorption edge at 5.5 µm. The InTlSb/InSb sample exhibits overall higher absorption, and an ab-
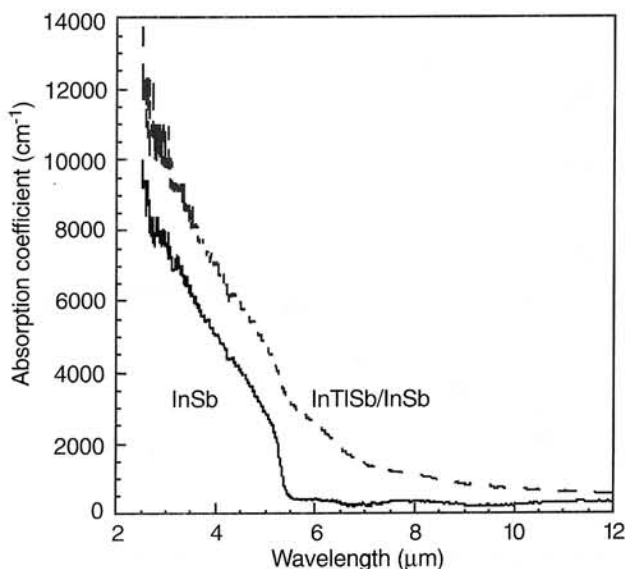

Fig. 6. Optical absorption spectra of InSb (solid line) and InTlSb (dashed line) extracted from transmission measurements.

sorption tail extending beyond InSb absorption edge is observed. It should be noted that the calculated absorption coefficient for InTlSb/InSb bilayer given in Fig. 6 corresponds to the average absorption of the two layers weighted by their respective thickness

$$\alpha = \frac{\alpha_{InTlSb} d_{InTlSb} + \alpha_{InSb} d_{InSb}}{d_{InTlSb} + d_{InSb}}, \quad (4)$$

where α_{InSb} and α_{InTlSb} designate the absorption coefficients of each individual layer. d_{InSb} and d_{InTlSb} correspond to their respective thickness. This tends to attenuate any feature of the InTlSb absorption spectrum, and the observed shift should be even more apparent for a thick InTlSb layer.

Figure 7 shows the spectral photoresponse from the InSb and $In_{1-x}Tl_xSb$ films grown on GaAs substrates. For the InSb sample, an absorption cutoff wavelength at about 5.5 µm was observed at 77 K, which agrees with the photoluminescence measurement [37]. The bump around 4.3 µm is due to the carbon dioxide absorption in the spectra. A distinct shift of absorption edge from 5.5 for InSb up to 8.4 µm for InTlSb was observed at 77 K. In general agreement with the theoretical prediction, the samples grown at higher Tl input flows exhibited longer response wavelengths. It is interesting to note that, as Tl incorporation increases, the degree of tailing of the photoresponse line becomes larger, which may be accounted for by the gradual increase of band edge perturbation due to vacancies, antisites, and other resid-
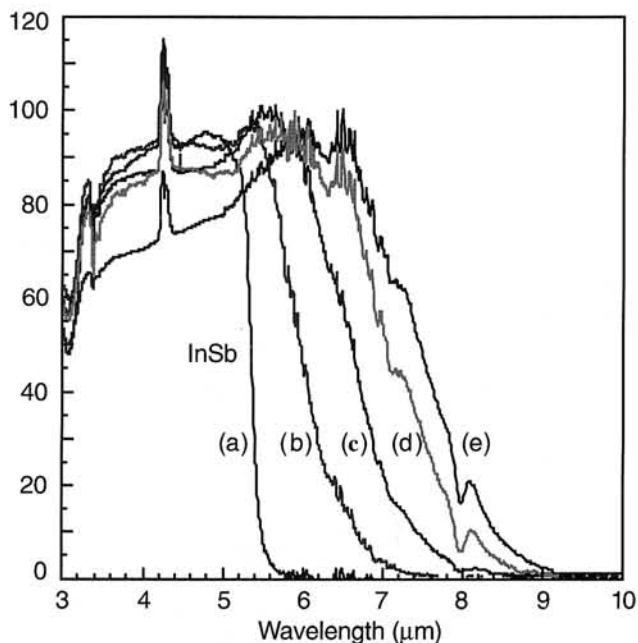
Fig. 7. Normalised spectral photoresponse of InSb and various $In_{1-x}Tl_xSb$ samples measured at 77 K. The estimated Tl contents are approximately (a) x = 0, (b) x = 0.025, (c) x = 0.036, (d) x = 0.044, and (e) x = 0.048.

Fig. 8. Room temperature Hall mobility (a) and electron concentration (b) as a function of 77 K photoresponse cutoff wavelength.

ual impurities [33,34]. The rough estimation of the solid Tl concentration in the samples has been made by linearly interpolating the energy band gap between InSb and TlSb from the fact that the band gap energy of the grown InTlSb is deviated only slightly from that of InSb. A cutoff wavelength (λ_c) of InTlSb was converted to band gap energy by the relation of $E_g = 1.24/\lambda_c$, where E_g is in eV and λ_c is in µm. Energy band gap of −1.5 eV at 300 K is assumed for the semimetal TlSb [13].

3.4. Electrical characteristics

A number of trends have been observed in the electrical properties of InTlSb. Hall measurements indicated a room temperature Hall mobility ranging from 50 000 to 20 000 cm²/Vs, and an electron concentration ranging from 1×10^{16} to 5×10^{16} cm⁻³ for the InTlSb samples, as shown in Fig. 8. The Hall mobility decreased monotonously with increasing Tl flow, while the electron concentration simultaneously increased. The increase in electron concentration is typical of an intrinsic semiconductor with decreasing band gap. The decrease of the mobility may be attributed to an increase of impurity and alloy scattering. Alloy scattering has been shown to be significant in other Sb-based compound such as InAsSb [38]. Measurements at 77 K indicate an opposite trend for the
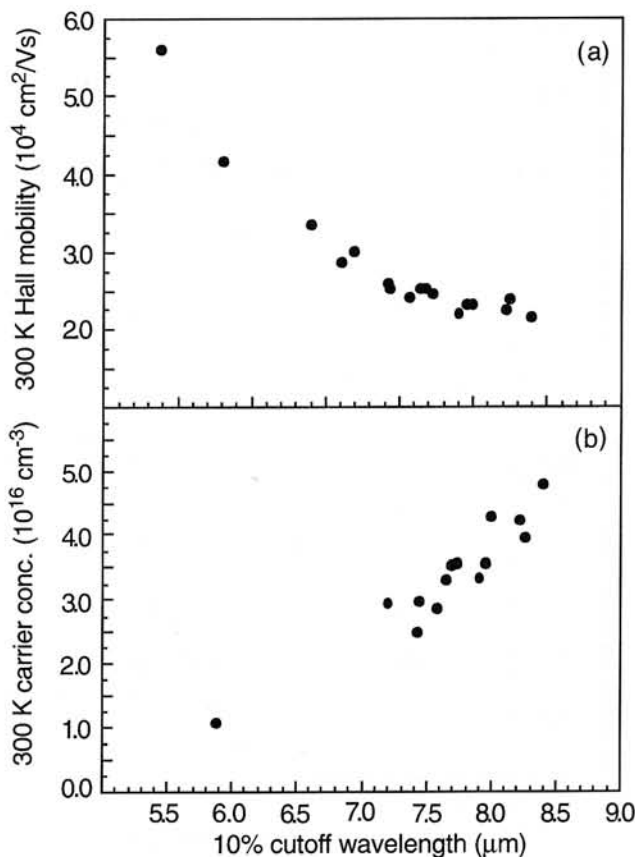
mobility and scattered data for electron concentration (Fig. 9). This behaviour is likely to occur because of the dominant contribution of parallel conduction layers at low temperature, as evidenced in InSb epilayers through temperature dependent Hall measurement [39].

4. InTlSb photodetectors

In this section, we describe the first demonstration of InTlSb infrared photodetectors fabricated on GaAs substrates. Preliminary photodetectors were operated in photoconductive mode. The photoconductors were rectangular shaped with dimension of 3×3 mm². Ti/Au were evaporated by an electron-beam evaporator to make contacts. Ti exhibits strong mechanical adhesion with semiconductor materials. The resistance is about 50 Ω at room temperature and increases up to several thousand Ω at 77 K. The spectral photoresponse is measured by a FTIR spectrometer with a low-noise preamplifier (Itacho 120). The responsivity is calibrated by a blackbody test setup, including a black body source (Mikron 305), pream-
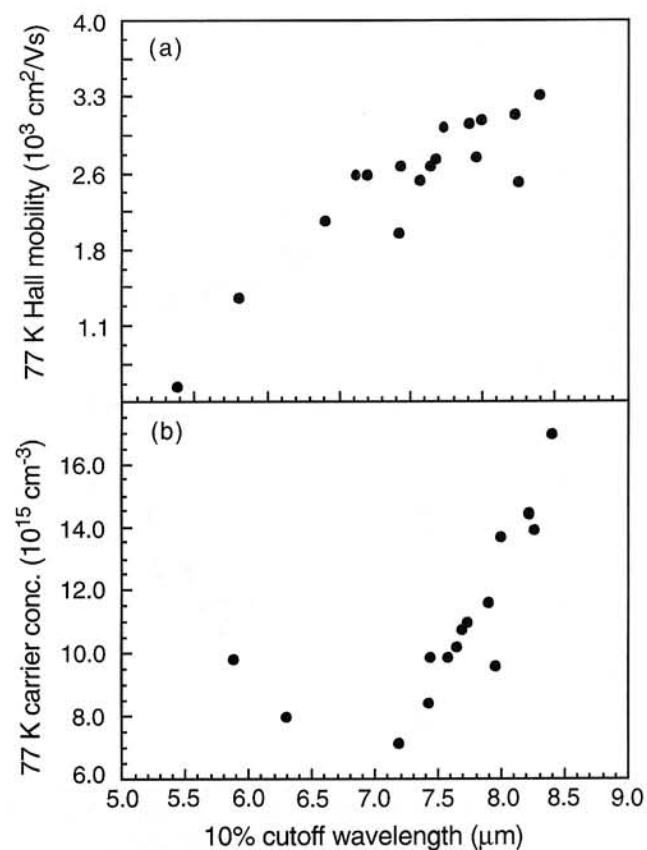
Fig. 9. 77 K Hall mobility (a) and electron concentration (b) as a function of 77 K photoresponse cutoff wavelength.

Fig. 10. The spectral responsivity of an $In_{0.94}Tl_{0.06}Sb$ photoconductor at 77, 200, and 300 K.

plifier (EG&G PA-6), and chopper system (Stanford Research System SR-540). The black body temperature is set at 800 K. The modulating frequency is set at 400 Hz since response measurements as a function of chopper frequency showed that the thermal effect could be neglected at frequencies higher than 200 Hz. The photodetectors were mounted in a liquid nitrogen cooled cryostat system and measurements were taken at temperatures between 77 K and 300 K.

The absolute responsivity for an $In_{0.94}Tl_{0.06}Sb$ photodetector is displayed in Fig. 10. The cutoff wavelength extends up to 11 µm at 300 K. The maximu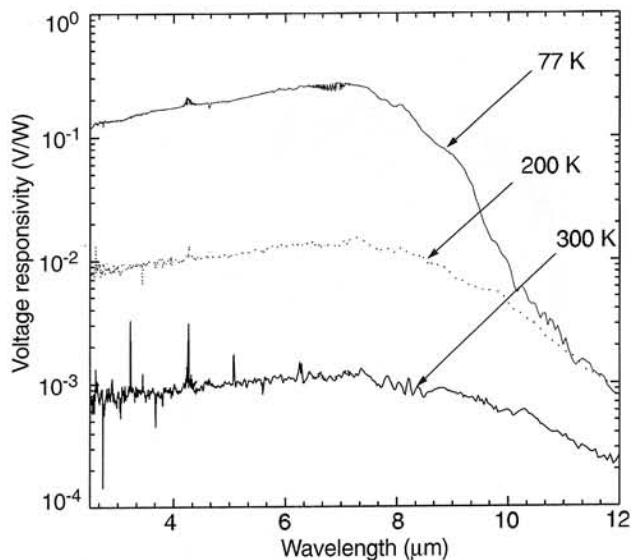m responsivity in an $In_{0.96}Tl_{0.04}Sb$ photodetector is about 6.64 VW^{-1} at 77 K. The corresponding Johnson-noise limited detectivity is 7.64×10^8 cmHz$^{1/2}$W^{-1}. The voltage responsivity and detectivity of $In_{1-x}Tl_xSb$ photoconductive detectors are listed in Table 3.

In order to obtain the carrier lifetime, the voltage dependent responsivity was measured. Figure 11 shows the voltage-dependent responsivity of InTlSb photodetectors. It increases with voltage, saturates at a given voltage, and finally decreases. The saturation of responsivity at large voltage can be explained by the sweep-out effect [3]. Based on the voltage responsivity, the electron mobility-effective carrier lifetime product $\mu_e\tau$ and effective carrier lifetime τ can be derived. According to the simple theory of photoconductivity, the voltage responsivity R_v can be expressed as [3]

$$R_v = \frac{q\lambda}{hc}\frac{\eta\mu_e\tau V_b R_D}{L^2}\left(1+\frac{1}{b}\right) \qquad (5)$$

where q is the electron charge, λ is the wavelength, η is the quantum efficiency, b is the electron-to-hole

Table 3. Performance of $In_{1-x}Tl_xSb$ photoconductors at 77 K.

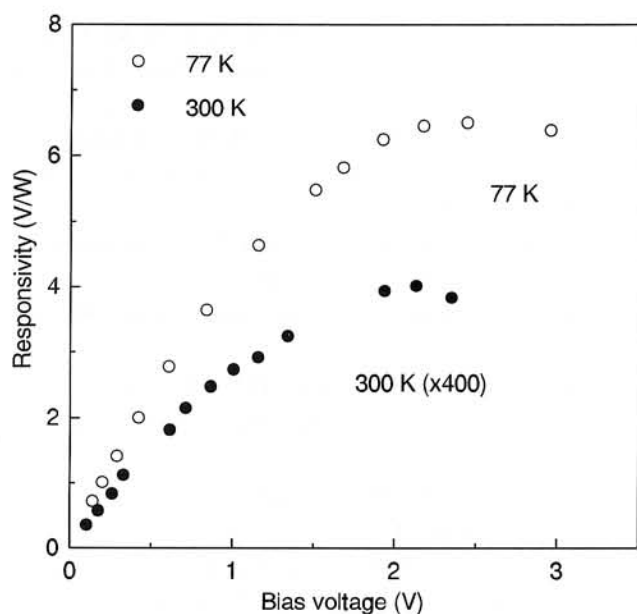| $In_{1-x}Tl_xSb$ detectors	$\lambda_{cut-off}$ (µm)	R_v^{max} (V/W)	D^*_{max} (10^8 cmHz$^{1/2}$/W)	μ (10^3 cm^2/Vs)	τ (ns)
x = 0.023	6.5	2.73	2.47	1.29	19.2
x = 0.035	7.3	6.64	7.64	2.00	50.1
x = 0.047	8.4	3.56	8.54	2.75	40.4
x = 0.053	9.4	0.79	2.63	4.13	10.3

Fig. 11. The voltage-dependent responsivity of an $In_{0.94}Tl_{0.06}Sb$ photoconductor.

mobility ratio, L is the detector length, V_b is the bias voltage, and R_D is the detector resistance. Assuming an internal quantum efficiency of ≈ 1, the quantum efficiency η has been calculated using [3]

$$\eta = (1-r)\frac{\left(1-e^{-\alpha t}\right)}{\left(1-re^{-\alpha t}\right)} \qquad (6)$$

where r is the reflectance, α is the absorption coefficient, and t is the thickness of the layer. The $\mu_e\tau$ product has been determined using Eq. (5). If μ_e is known τ can be estimated. The effective carrier lifetime τ in InTlSb epitaxial layers is listed in Table 3, which is 10-50 ns at 77 K and 0.1-0.6 ns at 300 K.

In spite of the large lattice mismatch between InTlSb and GaAs, the InTlSb photodetectors exhibited good characteristics at room temperature. The detector performance could be further improved by employing previously developed technologies for II-VI uncooled detectors such as optical immersion, resonant optical cavity, and suppression of Auger recombination [8].

5. Conclusions

High quality InTlSb films were successfully grown by LP-MOCVD technique for the first time using trimethylindium (TMI), trimethylantimony (TMSb), and cyclopentadienylthallium (CPTl) as the source materials.

The presence of Tl was confirmed by AES. The structural properties of InTlSb have been investigated using HRXRD. (004) x-ray diffraction peak that is attributed to $In_{1-x}Tl_xSb$ is clearly observed. However, the out-of-plane lattice parameter of the $In_{1-x}Tl_xSb$ gradually decreased with Tl incorporation, which can not be accounted for by atomic size effect. The present results also show that both the FWHM of HRXRD and the degree of tailing of the absorption edge gradually increase as Tl incorporation become heavier. We suggest that Tl incorporation in InSb induces overall defects and gives rise to residual tensile stress of the order of 10^4 N/cm^2.

Through optical transmission measurements, extension of absorption edge has been observed in the InTlSb layers. Infrared photoresponse measurements showed that the cutoff wavelength of the InTlSb alloys were tailored from 5.5 up to 8.4 µm at 77 K. The electrical properties of InTlSb epilayers were investigated by Hall effect measurements. Room temperature Hall mobility ranged from 50 000 to 20 000 cm^2/Vs and electron concentrations varied from 1×10^{16} to 5×10^{16} cm^{-3} with the increase of Tl concentration.

We also demonstrate the photodetectors fabricated from the grown InTlSb alloys. Photoresponse of InTlSb photodetectors is observed up to 11 µm at room temperature. The maximum responsivity of an $In_{0.96}Tl_{0.04}Sb$ photodetector is about 6.64 VW^{-1} at 77 K, corresponding to a detectivity of 7.64×10^8 cmHz$^{1/2}$W^{-1}. The carrier lifetime in InTlSb photodetectors derived from the stationary photoconductivity is 10-50 ns at 77 K. The experimental results showed the feasibility of using Sb-based alloys for the uncooled infrared photodetector applications.

Acknowledgments

References

1. E.L. Derenniak and G.D. Boreman, *Infrared Detectors and Systems*, John Wiley & Sons, New York, 1996.
2. W.L. Wolf and G.J. Zissis, *The Infrared Handbook*, ERIM, Ann Arbor, 1989.

3. A. Rogalski, *Infrared Photon Detectors*, SPIE Optical Engineering, Bellingham, 1995.

4. C.T. Elliott, *Handbook of Semiconductors*, Vol. 4, pp. 841–936, editted by T.S. Moss, North Holland, Amsterdam, 1981.

5. R.M. Broudy and V.J. Mazurczyk, *Semiconductors and Semimitals*, Vol. 18, pp. 157–199, editted by R.K. Willardson and A.C. Beer, Academic Press, New York, 1981.

6. N.T. Gordon, *Semi. Sci. Technol.* **6**, C107 (1991).

7. Z. Djuric, J. Piotrowski, Z. Jaksic, and Z. Djinovic, *Electron. Lett.* **24**, 1590 (1988).

8. J. Piotrowski and T. Niedziela, *Infrared Phys.* **30**, 113 (1990).

9. C.G. Bethea, B.F. Levine, M.Y. Yen, and A.Y. Cho, *Appl. Phys. Lett.* **53**, 291 (1988).

10. M.Y. Yen, *J. Appl. Phys.* **64**, 3306 (1988).

11. J.D. Kim, D. Wu, J. Wojkowski, J. Piotrowski, J. Xu, and M. Razeghi, *Appl. Phys. Lett.* **68**, 99, (1996).

12. J.D. Kim, S. Kim, D. Wu, J. Wojkowski, J. Xu, J. Piotrowski, E. Bigan, and M. Razeghi, *Appl. Phys. Lett.* **67**, 2645 (1995).

13. M. Schilfgaarde and A. Sher, *Appl. Phys. Lett.* **62**, 1857 (1993).

14. Y.H. Choi, C. Besikci, R. Sudharsanan, and M. Razeghi, *Appl. Phys. Lett.* **63**, 361 (1993).

15. Y.H. Choi, P.T. Staveteig, E. Bigan, and M. Razeghi, *J. Appl. Phys.* **75**, 3196 (1994).

16. A.M. Jean-Louis and C. Hamon, *Phys. Status Solidi.* **34**, 329 (1969).

17. J.L Zilko and G. E. Greene, *Appl. Phys. Lett.* **33**, 254 (1978).

18. A.J. Noreika, W.J. Takei, M.H. Francombe, and C.E.C. Wood, *J. Appl. Phys.* **53**, 4932 (1982).

19. J.J. Lee, J.D. Kim, and M. Razeghi, *Appl. Phys. Lett.* **70**, 3266 (1997).

20. J.J. Lee, J.D. Kim, and M. Razeghi, *Appl. Phys. Lett.* **71**, 2298 (1997).

21. J.J. Lee, J.D. Kim, and M. Razeghi, *Appl. Phys. Lett.* **73**, 602 (1998).

22. K.Y. Ma, Z.M. Fang, D.H. Jaw, R.M. Cohen, and G.B. Stringfellow, *Appl. Phys. Lett.* **55**, 2420 (1989).

23. M.V. Schilfgaarde, A.B. Chen, S. Krishnamurthy, and A. Sher, *Appl. Phys. Lett.* **65**, 2714 (1994).

24. C. Wood, A. Noreika, and M. Francombe, *J. Appl. Phys.* **59**, 3610 (1986).

25. R.S. Williams, *Z. Anorg. Allg. Chem.* **50**, 127 (1906).

26. T. Barth, *Z. Phys. Chem.* **127**, 113 (1927).

27. E. Persson and A. Westgren, *Z. Phys. Chem.* **136**, 208 (1928).

28. L.J. Sham and M. Schluter, *Phys. Rev. Lett.* **51**, 1888 (1983).

29. J.C. Phillips, *Bonds and Bands in Semiconductors*, Academic Press, New York, 1973.

30. L.D. Landau and E.M. Lifshitz, *Theory of Elasticity*, Pergamon, Oxford, 1970.

31. D.L. Smith, *Thin Film Deposition: Principles and Practice*, McGraw Hill, New York, 1995.

32. M. Leszczynski, H. Teisseyre, T. Suski, I. Grzegory, M. Bockowski, J. Jun, K. Pakula, J.M. Baranowski, C.T. Foxon, and T.S. Cheng, *Appl. Phys. Lett.* **69**, 73 (1996).

33. E.J. Tarsa, E.A. Hachfeld, F.T. Quinlan, J.S. Speck, and M. Eddy, *Appl. Phys. Lett.* **68**, 490 (1996).

34. W. Buckel, *J. Vac. Sci. Technol.* **6**, 606 (1969).

35. Q. Du, J. Alperin, and W.I. Wang, *J. Cryst. Growth* **175**, 849 (1997).

36. Landolt-Bornstein, *Numerical Data and Functional Relationships in Science and Technology*, Vol. 17, Springer-Verlag, New York, 1982.

37. E. Michel, J. Xu, J.D. Kim, I. Ferguson, and M. Razeghi, *IEEE Photonics Technol. Lett.* **8**, 673 (1996).

38. V.W.L. Chin, R.J. Egan, and T.L. Tansley, *J. Appl. Phys.* **69**, 3571 (1991).

39. C. Besikci, Y.H. Choi, R. Sudharsanan, and M. Razeghi, *J. Appl. Phys.* **73**, 5009 (1993).